Fuel 404 (2026) 136339

Contents lists available at ScienceDirect

Fuel

journal homepage: www.elsevier.com/locate/fuel

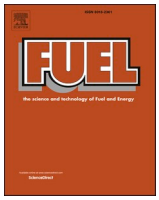

Full Length Article

Realistic electrolyzer temperature and pressure conditions evaluation of NiFeP/Zn-coated electrodes for alkaline water splitting

Jhaniel Osorio, Simón G. Quiroz, Santiago Cartagena, Jorge A. Calderón *

Centro de Investigación, Innovación y Desarrollo de Materiales – CIDEMAT, Universidad de Antioquia, Cr. 53 No 61 – 30, Torre 2, Lab. 330, Medellín, Colombia

ARTICLE INFO

Keywords:
Hydrogen evolution
Oxygen evolution
Water electrolysis
Elevated Temperature and Pressure
Electrodeposited coatings

ABSTRACT

The current transition to renewable energies has motivated research into energy storage using various techniques. Of these, electrolysis for pure hydrogen production stands out, as hydrogen is a crucial energy vector molecule capable of decarbonizing multiple sectors. However, the low efficiency of the electrolysis process presents a major limitation. In this work, an electrochemical evaluation of catalyst materials for water splitting under elevated temperature and pressure (ETP) conditions to replicate realistic electrolyzer operating environments is proposed. The NiFeP/Zn-coated nickel foam electrodes demonstrated a brain-like compact morphology, with EDS revealing a composition of 62.20 at% Ni, 13.90 at% Fe, 1.60 at% Zn, 7.65 at% P, and 15.21 at% O_2. Electrochemical performance tests revealed a significant reduction in overpotential for the hydrogen evolution reaction (HER), achieving 38 mV at 8 bar and 80 °C, while the oxygen evolution reaction (OER) exhibited 119 mV at 1 bar and 80 °C, both at |30| $mAcm^{-2}$. Chronopotentiometry confirmed the stability of the coating for over 24 h at high current density of |400| $mAcm^{-2}$. The bifunctional capability of the coating was validated in a full-cell test, obtaining a remarkably low overpotential of 1.47 V at 30 $mAcm^{-2}$ for overall water splitting under 80 °C and 8 bar conditions.

1. Introduction

In recent years, the penetration of wind, solar, and other form of energy derived from renewable sources into the electrical grid has increased. This represents a reduction of about 40 % in the equivalent CO_2 generated from the energy matrix [1], leading to much cleaner energy consumption. However, there are still some significant issues to solve.

The intermittent behavior of the sources used in these systems (sun radiation and wind) leads to intermittent energy production. These sources cannot supply enough energy to meet consumption requirements consistently. As a result, there is a need to store energy that can be used when the grid requires it to satisfy demand. The most used method worldwide to balance the energy grid through energy storage is mechanical storage. This involves pumping water and compressing air when energy consumption is low, resulting in the storage of "cheap" energy. Electrochemical storage (using batteries) has also gained popularity due to its efficiency and pollution-free operation [2–4]. In recent years, chemical storage using green hydrogen and other molecules has emerged as a leading area of research. This is due to its promising properties as an energy vector that can facilitate the energy transition [5]. Green hydrogen helps stabilize the grid and supports the decarbonization of various industries [6–8]. It is produced through the electrolysis of water into H_2 and O_2 using renewable electricity and offers advantages compared to the storage methods mentioned earlier. As a molecular substance, H_2 can be commercialized in kilograms, pumped into pipelines, and even burned to generate heat. Additionally, it can be blended as $H_2 + CH_4$ or using other fuels and combustibles [9,10], which encourages a smoother transition to a cleaner society.

The primary drawbacks of green hydrogen production lie in the high cost and low efficiency of the electrolysis process. Therefore, to enable widespread adoption of clean hydrogen production, two key issues need to be addressed: the minimization of ohmic losses in the process and the reduction of the materials costs associated with electrolysis [11–14].

There are different approaches to addressing the two issues presented above. Some researchers are working on the development of novel materials with abundant metals (to reduce costs) that can catalyze the splitting reaction, thus reducing the extra electric energy (overpotential – η) required for the hydrogen evolution reaction (HER) or the oxygen evolution reaction (OER) [15–17]. Additionally, they are

* Corresponding author.
E-mail address: andres.calderon@udea.edu.co (J.A. Calderón).

https://doi.org/10.1016/j.fuel.2025.136339
Received 29 May 2025; Received in revised form 13 July 2025; Accepted 21 July 2025
Available online 26 July 2025

focused on increasing corrosion resistance [18–20]. Other researchers are focusing on technical considerations such as geometrical aspects, fluid dynamics within the electrolyzer [21], electrolyte behavior [22,23], and exploring thermodynamic and kinetics approaches using computational modeling [24]. However, the behavior of catalysts and electrodes under more severe conditions, especially those similar to electrolyzer operation, has been poorly investigated. Only a reduced number of studies have explored temperature and pressure conditions different to room or standard conditions. Leuaa et al. [25], for example, studied a CoO_X-coated Ni foam under high temperature and pressure (HTP) conditions (up to 150 °C and 45 bar) in 45 % wt KOH for the OER. They compared the performance of the CoO_X/NF system with commercially available electrodes, finding interesting stabilities along prolonged assessments of 185 mV at 500 mA cm^{-2}. Two additional studies have explored the effects of increasing temperature for OER catalysis, although detailed information about overpotentials was limited. Abdelghafar et al. [26] assessed a BSCF perovskite between 25–60 °C, while Czioska et al.[27] worked with an IrO_2 system that was evaluated using temperatures up to 80 °C. The IrO2 study was primarily focused in structural changes and oxidation behavior rather than benchmarking performance.

The effects of modifying temperature and pressure on HER and OER have thermodynamic and kinetic implications. Increasing the evaluation temperature affects the reaction's equilibrium position and reversible potential, as described by the Nernst equation [12]. The temperature increase also improves electrolyte conductivity, a crucial factor in enhancing reaction efficiency, allowing ions to move easily between electrodes [23,24,28–30]. In addition, increasing pressure in hydrogen production can reduce costs by decreasing the need for extensive post-compression of the resulting gas to achieve competitive energy density and improve bubble management during the electrolyzer operation. However, the idea of a pressurized system evokes varying opinions among researchers, as presented by Jang et al. [13]. According to their findings, higher pressure allows a higher temperature evaluation, maintaining water in a liquid state, and facilitating the production of purer hydrogen without the need for a water adsorption device. Nonetheless, there is a significant drawback: if the effect of pressure is considered independently, an increase in the pressure system raises the equilibrium potential of the reaction, meaning more energy is required in the full cell. Although pressure is most frequently discussed in relation to thermodynamics, it also affects other kinetic aspects including bubble behavior [31–33].

This work aims to investigate the behavior of a previously developed NiFeP/Zn material obtained [34] under more realistic temperature and pressure electrolyzer conditions. This material has shown promising overpotential results for HER and OER under standard laboratory conditions. Tests at elevated temperature and pressure (ETP), rather than standard laboratory conditions, will provide insights into the behavior of the material in practical applications and contribute to the development of a more efficient, in-house electrolyzer for future applications.

2. EXPERIMENTAL

2.1. Electrodes preparation

Open-pore nickel foam was used as the substrate for the electrode, taking advantage of its large surface area and its catalytic properties in alkaline water electrolysis. The use of foams has several drawbacks when evaluating the proper catalytic behavior of the coatings, as Zheng et al. describe [35]. The areas that most commonly lead to mistakes are surface area evaluation, current density normalization and experimental setup (capillarity, other materials in foam holders and undefined area). For this work, a TMAX 1.6 mm thick Ni foam was used, with a porosity of 97 % and a purity of 99.8 %. Ni foam rectangles of 2.5 cm^2 were cut out, and the area for evaluation was determined as 1 cm^2. The rest of the electrode was used for connections with the potentiostat. To avoid capillarity into the connecting area of the electrode epoxy resin was used to fill the pores and the foam was slimmed down in two points before the resin application, as shown in Fig. 1.

2.2. Catalytic coatings synthesis

Before the electrodeposition process of the catalytic coatings, the foams were activated in an ultrasonic bath using HCl 3 M for 5 min, to remove passive layers and oxides from the surface of the electrode. After the process the foams were rinsed with type III water (conductivity < 2.5 μScm^{-1}).

The NiFeP/Zn catalytic coatings were electrodeposited based on a previous work [34], with some adjustments for the new substrate (nickel foam). The counter electrode used was a Pt mesh, applying a current density of –200 mA cm^{-2} to the working electrode for 2400 s using an AUTOLAB PGSTAT302F potentiostat. The electrochemical bath was made up of type III water with 0.114 M $NiSO_4{\cdot}6H_2O$ (EMSURE® MERK, ≥ 99.0 %), 0.108 M $FeSO_4{\cdot}7H_2O$ (CARLO ERBA, ≥ 99.5 %), 0.102 M CH_3COOK (EMSURE® MERK, ≥ 99.0 %), 0.094 M $NaH_2PO_2{\cdot}H_2O$ (ALDRICH, ≥99 %) and 0.104 M of $ZnSO_4{\cdot}7H_2O$ (EMSURE® MERK, ≥ 99.5 %). The purpose of the increase in the current density and the Zn concentration was to increase the specific area of the substrate, aiming to obtain a similar behavior to that previously achieved on a stainless-steel planar substrate. The pH of the bath was adjusted to 2 with sulfuric acid for better Fe^{2+} stability and phosphorous behavior [36]. Bath agitation was carried out using air bubbles. After the electrodeposition, the electrodes were rinsed with type III water and treated with 6.0 M NaOH at room temperature for 24 h to leach the deposited Zn and create voids and increase surface area.

2.3. Material characterization

The chemical composition of the obtained coatings was evaluated through Raman spectroscopy, taken in a Horiba Jobin Yvon (Labram HR) Nikon (BX41) microscope, with a CCD detector (Wright 1024 × 256 pixels) and a 625 nm laser. Crystal structure was characterized by X-ray diffraction (XRD) using a Miniflex600 Rigaku device with CuK_α (λ = 1.54059 Å) as source, operated with a source power of 40 kV, and a 2θ scan from 10° to 80°. The morphology of the electrodes was characterized by scanning electron microscopy (SEM) and electron dispersive X-ray spectroscopy (EDS) JEOL-JSM 6490LV with accelerating voltage of 20 kV.

2.4. Electrochemical evaluation

Electrochemical experiments for water splitting (HER and OER) were carried out in triplicate using three different samples to obtain a statistical representation of the catalytic behavior. The experiments were divided into two parts, standard laboratory conditions and ETP conditions:

Experiments in Standard Laboratory Conditions

The performed assessments were carried out using an AUTOLAB PGSTAT302F potentiostat/galvanostat. A custom cell, with a volume of 80 cm^3 of NaOH 1.0 M, was used for all measurements and the foam was submerged up to the dash line shown in Fig. 1d). The electrodes used were a graphite rod as counter electrode and a Hg|HgO 0.098 V vs standard hydrogen electrode (SHE) as reference electrode, which was made in-house. The distance between the cathode and anode electrodes was approximately 25 mm.

Cyclic voltammetry (CV) to assess stability in the surface behavior was carrying out from 0.20 V to 0.70 V and −0.90 V to −1.40 V vs Hg|HgO respectively at a rate of 0.1 Vs^{-1}. Then, linear sweep voltammograms (LSV) were executed from 0.20 V to 1.10 V vs Hg|HgO for OER and from −0.40 V to −1.80 V vs Hg|HgO for HER at a scan rate of 5 mVs^{-1}, both with respect to the reference electrode. The analyses of

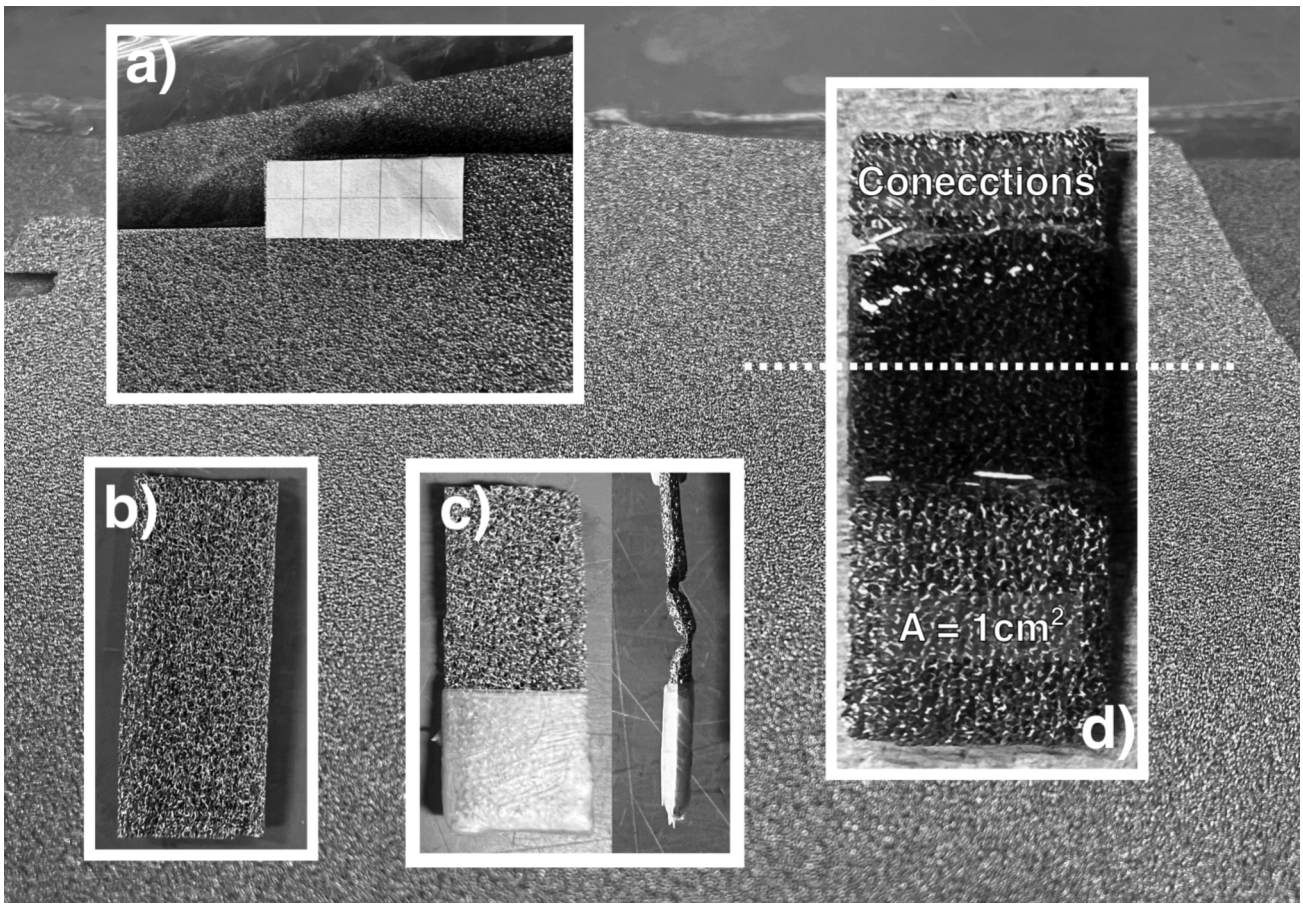

Fig. 1. Ni foam electrodes making process. a) Selection of 2.5 cm^2 area, b) Cut foam for the electrode, c) Definition of analysis area (1 cm^2) and slimed down points and d) Final electrode with resin.

stability and durability of the electrodes (chrono-potentiommetry) were carried out at a high current density of 400 $mAcm^{-2}$ for 24 h, which are the approximate conditions in which a real electrolyzer could work.

The potential values with respect to reversible hydrogen electrode were calculated as follows:

$$E_{RHE} = E_m + E_{ref/H2} + (0.059\,V \times pH) - (R_{sln} \times I) \quad (1)$$

The overpotential values were calculated as follows:

$$\eta = E_{RHE} - E_{eq} \quad (2)$$

Where, E_m is the measured potential, $E_{ref/H2}$ is the potential difference between the reference electrode and the SHE at 25 °C, I is the current response of the working electrode, R_{sln} is the solution resistance and E_{eq} is the equilibrium potential of the reaction (for HER 0 V; for OER 1.229 V).

Experiments in ETP Conditions

The ETP assessment was carried out using an autoclave from CORTEST adapted to hydrogen evolution experiments, with a cylinder with volume capacity of 5 L, which was able to withstand pressures and temperatures up to 35 MPa and 300 °C. To reach the appropriate evaluation pressure, gas inlet and outlet lines were adapted for pressurization. See Fig. S1 and Fig. S2 in the supporting information for details of the autoclave arrangements for ETP measurement conditions.

The autoclave electrodes were adapted in order to evaluate the coated foams developed (Fig. S2.). A Teflon holder was used to support the working electrode within the vessel, and a nickel-coated stainless steel metallic contact was used to reduce distortion of the results. A smaller version of the Hg|HgO electrode was developed (0.090 V vs Ag|AgCl) and a Pt spiral filament was used as counter electrode. LSV measurements were carried out using an AUTOLAB VIONIC device from 0.20 V to 1.10 V for OER and from −0.40 V to −1.80 V for HER at a scan rate of 5 mVs^{-1}, both with respect to the reference electrode, after a chrono-amperometry for 10 min using |10| mA. A temperature scan from 20 °C to 80 °C was conducted, with additional measurements up to 120 °C where the pressure conditions allowed for the assessment using liquid water and where good repeatability was achieved. These temperature ranges were selected according to operating conditions for typical alkaline electrolyzers and the maximum upper limits for anion exchange membranes [37–39]. Pressure conditions were varied between 1 bar, 4 bar and 8 bar to investigate the impact of incremental pressure changes on the system performance. A stability measurement for 24 h was performed at the end of the assessment using a chrono-potentiommetry at |400| $mAcm^{-2}$ for both HER and OER reactions. The agitation system of the autoclave was activated during chrono-potentiometry assessments using a speed of 70 rpm.

To account for thermodynamics shifts due to non-standard temperature and pressure differences, an additional mathematical correction is required. For pressures below 10 bar, the gas phase behavior can be approximated using ideal gas laws, as determined by Onda et al [40]. For higher pressures, more precise corrections are required. Based on a reference pressure of 1 bar, P. Millet proposed the following equation to calculate the reversible potential under elevated pressure [41]:

$$E_{(T,P)} = E_{(T,1)} + \frac{3*R*T}{4*F} ln(P) \quad (3)$$

Where $E_{(T,P)}$ is the reversible potential at a temperature T and at a pressure of 1 bar, R is the gas constant (8.314 J/molK), F is the Faraday

constant (96485C/mol e$^-$) and P is the pressure of the system in bar. To account for the temperature dependent shifts at 1 bar, the empirical equation proposed by LeRoy is used [42]:

$$E_{(T,1)} = 1.5184 - 1.5421*10^{-3}T + 9.523*10^{-5}T*ln(T) + 9.84*10^{-8}T^2 \quad (4)$$

Additionally, the Hg|HgO (0.098 V vs SHE at ~ 25 °C) reference electrode used in the system also requires a correction to determine a better $E_{ref/H2}$ term presented in *equation (1)*. Using the Nernst equation, this correction is calculated as follows [[43,44],]:

$$E_{Hg,HgO} = E^{\circ}_{Hg,HgO}(T) - \frac{RT}{2F} ln\left(\frac{\alpha^2_{OH^-}}{\alpha_{H_2O}}\right) \quad (5)$$

$$E^{\circ}_{Hg,HgO}(T) = 0.0980 - 1.120x10^{-3}(T-298) - 3.388x10^{-6}(T-298)^2 \quad (6)$$

The activity of water in the NaOH solution is defined as a function of temperature and molality m (mol/kg$_{H2O}$) as mentioned by Balej [45]:

$$\alpha_{H_2O} = 10^{\left(-0.01332m+0.002542m^2-3.06x10^{-5}m^3+\frac{1.5827m-1.5669m^2+0.021296m^3}{T}\right)} \quad 7)$$

The activity coefficient of NaOH (γ_{NaOH}) can be calculated using the following equations, where t_p is the solution temperature and m is the molality.

$$log(\gamma_{NaOH}) = \frac{-u\sqrt{m}}{1+\sqrt{2m}} + Bm + Cm^2 + Dm^3 + Em^4 \quad (8)$$

$$B = 0.006519 + 0.0015995t_p - 0.000018327t_p^2 \quad (9)$$

$$C = 0.013713 - 0.00050071t_p + 0.0000056385t_p^2 \quad (10)$$

$$D = 0.0005994 + 0.000050215t_p - 0.00000064754t_p^2 \quad (11)$$

$$E = -0.00000596 - 0.0000018056t_p + 0.000000024073t_p^2 \quad (12)$$

$$u = 8.00x10^{-6}t_p^2 + 0.0005t_p + 0.4874 \quad (13)$$

$$\alpha_{OH} \approx \gamma_{NaOH} m_{NaOH} \quad (14)$$

2.5. Energy efficiency coefficient Determination and specific energy consumption

The energy efficiency of the electrolysis is a critical point in determining the overall cost of hydrogen production [46]. Given the operational variations outlined in this study, energy efficiency is expected to vary in the full cell evaluation. According to Faraday's law, the hydrogen production rate (ṁ) is directly proportional to the charge transfer flow and can be expressed as follows (in g/s):

$$\dot{m} = \frac{I_{cell}PM}{zF} \quad (15)$$

Where I_{cell} is the current of the cell (A), PM is the molar mass of hydrogen (g/mol), F is Faraday's constant (96485 A*s/mol), and z represents the number of transferred electrons. The specific energy consumption (E_s) of the electrolyzer is the relationship between the consumed electrical energy and the amount of hydrogen produced. Considering only the electrolysis process under the varying operational conditions, E_s can be determined as follows [47–50]:

$$P_{cell} = V_{cell}I_{cell} \quad (16)$$

$$\dot{m} = \frac{P_{cell}PM}{V_{cell}zF} \quad (17)$$

$$E_s = \frac{P_{cell}}{\dot{m}} = \frac{V_{cell}zF}{PM} \quad (18)$$

Where P_{cell} is the power consumption (W) and V_{cell} is the cell voltage (V). Thus, the specific energy consumption can be simplified to:

$$E_s\left[\frac{kWh}{kgH_2}\right] = V_{cell}*26.589 \quad (19)$$

$$E_s\left[\frac{kWh}{Nm^3}\right] = V_{cell}*2.392 \quad (20)$$

The energy efficiency (η_E), is subsequently derived by taking the ratio of the chemical energy contained in the produced hydrogen to the electrical energy consumed during water electrolysis. Consequently, the efficiency can be calculated using the higher heating value (HHV) of hydrogen (39.4 kWh/kgH_2 [49]) and the previously calculated energy consumption (KWh/kgH_2), as follows [47–50]:

$$\eta_E = \frac{HHV\ of\ H_2}{E_s} \quad (21)$$

3. Results and discussion

3.1. Coating characterization

A morphological coating evaluation was performed with SEM images, and the results are shown in Fig. 2, where the micrographs show the different stages that the electrode presents until the final catalyst is obtained. The uncoated nickel substrate is shown in Fig. 2(a) and Fig. 2 (b), where the surface of the electrode tends to be very smooth and uniform, and only irregularities from the metal grains and fabrication flaws are observed. Once the NiFePZn (unleached) coating is applied to the electrode, it is possible to observe the formation of a fairly homogeneous coating, which is shown in Fig. 2(c) and Fig. 2(d) at different magnifications. The coating forms clusters with an average diameter of 10.88 ± 1.96 μm, which are themselves formed of smaller particles of 0.84 ± 0.17 μm. Despite the distribution of the deposition, there are some clusters concentrated toward the borders of the nickel foam, which may be related to a localized increase in current density (edge effect phenomenon). After the leaching process to form the NiFeP/Zn coating (Fig. 2(e) and Fig. 2(f)), it was possible to obtain a compact surface with the conventional brain-like morphology of this type of catalyst, which resembles the surface of a coral due to the formation of valleys, peaks and discontinuities, with the presence of randomly distributed disperse elongated clusters. This morphology is obtained due to the elimination of Zn on the surface, which promotes an increase in surface area, generating more catalytic spaces for the water splitting reaction, as discussed in more detailed in previous work [34]. Some measures were considered to avoid degradation associated with the discontinuities formation during the leaching process and to validate the stability and the integrity of the catalytic coating, like: i) the selection of a reliable Zn concentration in the electrochemical bath for good catalytic behavior and good stability. ii) Alkaline corrosion stability studies using on/off tests, EIS and OCP measurements in the alkaline medium operating at high current densities like 400 mAcm^{-2}.

Chemical composition analysis of the deposited coating was performed to identify the catalytic species present in the system. Additionally, the presence of Ni-O, Fe-O and Ni-P interactions in the NiFeP/Zn coating system are expected. These interactions were previously identified in more detail in our earlier study [34], where ex-situ and in-situ Raman spectroscopy confirmed the formation of NiOOH during electrode polarization. However, this species could not be detected in the absence of polarization. Additionally, XPS analysis confirmed the presence of other additional species such as $Ni(OH)_2$, NiP_2, FeOOH and Fe_2O_3 [34].

According to the X-ray spectroscopy (EDS) results (Table 1), the

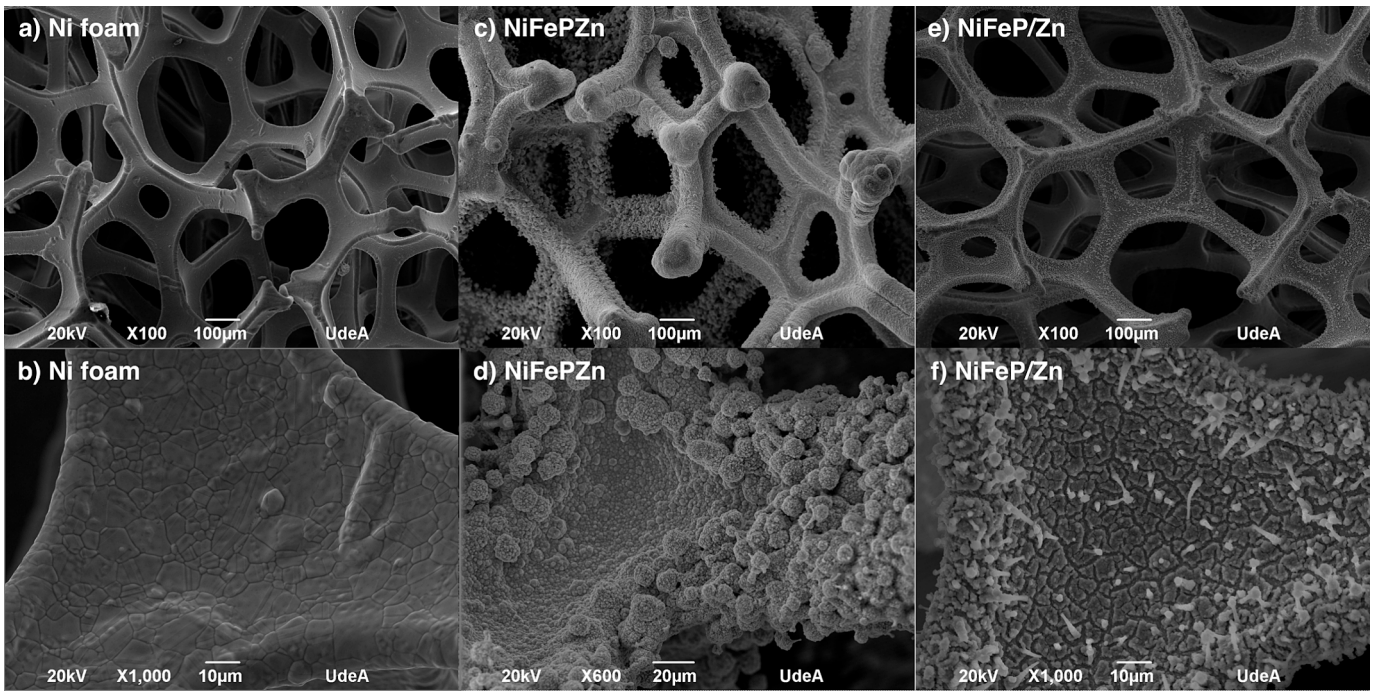

Fig. 2. SEM micrograph for foams electrodes. a) Nickel foam at X100, b) Nickel foam at X1000, c) NiFePZn coating unleached at X100, d) NiFePZn coating unleached at X600, e) NiFeP/Zn coating leached at X100 and f) NiFeP/Zn coating leached at X1000.

Table 1
Atomic percent results from EDS analysis.

NiFePZn		NiFeP/Zn (after leaching process)	
Element	Atomic percent (%)	Element	Atomic percent (%)
Ni	5.29	Ni	62.62
Fe	0.97	Fe	13.90
Zn	93.39	Zn	1.60
P	0.36	P	7.65
O	–	O	15.21

NiFeP/Zn leached coating exhibits a high content of Ni (62.62 at%) compared to the other elements used in the electrodeposition bath. This behavior was expected not only because of the use of an Ni substrate, but also because it aligns with previous research results, where the leaching process showed two different actions in the catalyst conformation; it participates in the remotion of a significant content of Zn from the coating, and also acts as a surface treatment that modifies the interaction of the other elements [34]. In this case, the Fe content in the final coating was 13.90 at%, Zn was only 1.60 at%, and phosphorus and oxygen were 7.65 at% and 15.21 at% respectively. In the same vein, the X-ray diffraction (XRD) results shown in Fig. 3(a) suggest an important participation of Ni in the coating, since the diffractogram obtained for the NiFeP/Zn coating only shows peaks associated with Ni based compounds. The strong peaks at 2θ of 44.3°, 52.1° and 79.8° are associated with the planes (1 1 1), (2 0 0) and (2 2 0) respectively, of the FCC structure in the metallic Ni (ICDD:00–004-0850) [51,52]. This pattern is mostly related to the nickel foam substrate. Some other peaks at 2θ of 37.2° and 43.7°, associated with the planes (1 1 1) and (2 0 0), are from the Ni_8Zn_2O compound (ICDD:01–075-0271). Meanwhile the peak at 2θ of 62.7° is associated with plane (2 2 0) of NiO (ICDD:00–004-0850) [51,52]. Additionally, some less intense peaks at 2θ 19.12°, 35.52°,

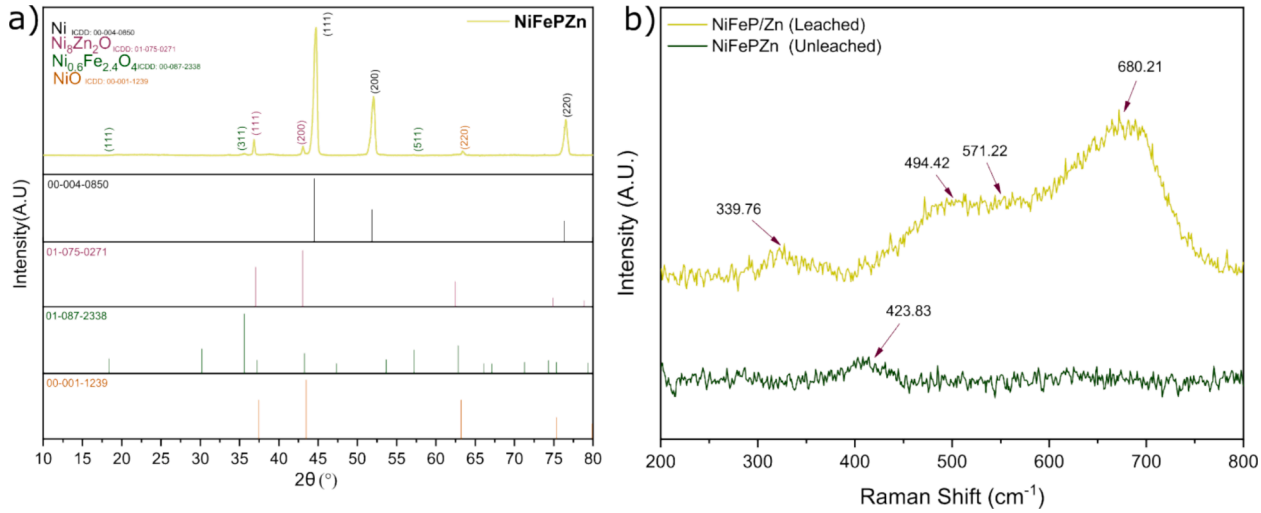

Fig. 3. a) X-ray diffractogram for Ni and NiFeP/Zn, b) Raman spectra obtained for the coating.

57.24° associated with the planes (1 1 1), (3 1 1) and (5 1 1) are from a $Ni_{0.6}Fe_{2.4}O_4$ compound (ICDD: 01–087-2338).

Additionally, the vibrational response spectra of the coating, both before and after leaching process, is shown in the Raman spectra of Fig. 3 (b). The unleached NiFePZn layer showed a high fluorescence, possibly related to metal-like behavior of the substrate and the coating, even though one band is observed at 423.83 cm^{-1}. This band could be associated with one of the characteristic bands of ZnO that usually presents before 440 cm^{-1} [53,54]. Once the deposited layer is leached, the metallic-like behavior is reduced and new bands are formed at 339 cm^{-1}, 494 cm^{-1}, 571 cm^{-1} and 680 cm^{-1}, which are associated with the vibrational responds of Ni-Zn ferrites [55], especially the Zn-O stretching and Ni-O bonds [55,56]. New bands that are formed following the leaching process provide additional proof that, in addition to removing the majority of Zn from the surface, this procedure also enriches the layer by forming different catalytic species, similarly to an aging treatment.

The formation of the NiFeP/Zn quaternary system as catalytic coating for alkaline water splitting combines different strategies to enhance the catalytic behavior of NiFe-based alloys. Ni and Fe act as the main electrocatalytic centers for HER and OER after leaching, forming Ni-O, Fe-O and Ni-P species. Additionally, as confirmed in our previous study [34], using in-situ Raman spectroscopy and XPS, NiOOH and FeOOH catalytic species are formed during polarization under alkaline conditions. P induces the formation of an amorphous structure, that improves catalytic performance and corrosion resistance. Zn is a sacrificial element, which after remotion from the surface during the leaching process, generates a high-surface-area, which increases electroactive sites.

3.2. Electrochemical evaluation

The electrochemical behavior of the NiFeP/Zn coating deposited on Ni foams for HER and OER was evaluated to determine the activity and durability under various conditions. The evaluation was conducted using linear sweep voltammetry and chronopotentiommetry under both room laboratory conditions (20 °C and 1 atm) and at ETP conditions, to identify the differences in the response of the material when assessed under real electrolyzer conditions.

3.2.1. Laboratory conditions

The corrected polarization curves of the LSV results for the bifunctional coating are shown in Fig. 4. Both the cathodic and anodic results exhibited good catalytic activity, with overpotentials of 96 mV for hydrogen evolution and 258 mV for oxygen evolution at |30| $mAcm^{-2}$. These values are consistent with the previously obtained overpotentials on flat AISI 304 stainless steel electrodes [34], but with a notable reduction associated with the high active surface area of the electrode. For HER, the obtained overpotential is comparable to those recently reported by Shan et al. [57] and Mathew et al [58] at |10| $mAcm^{-2}$, such as NiFeP nanosheets (94 mV), NiFe-LDH (113 mV), $FeNi_3N$/NF (75 mV), $NiCoFe_XP$/CC (39 mV), FeCoNiP@NC (187 mV), and for 20 % Pt/C (47 mV) as shown for Chen et al [59]. For OER, the obtained overpotential is within the range of other efficient systems. For instance, nanostructured amorphous NiFeP exhibited an overpotential of 248 mV at |50| $mAcm^{-2}$ [60], while NiFe-LDH (15:1) exhibited a value of 206 mV at |30| $mAcm^{-2}$ [61]. A recent review reported by Xiao et al. [62] highlights values that ranged from 204 mV (SONFO NS) to 370 mV ($NiSn(OH)_6$) measured at |10| $mAcm^{-2}$, and the benchmark of RuO_2 on CC of 274 mV at |10| $mAcm^{-2}$ [59].The combination of low overpotentials for both HER and OER in the current work confirms the bifunctional nature of NiFeP/Zn for alkaline water electrolysis, which is essential for scalability of electrolyzers of overall water splitting applications. Furthermore, as noted by Shan et al. [57], electrodeposition offers a promising option for scaling up coatings for industrial applications.

The stability of the coating was evaluated by 24 h at a current density of |400| $mAcm^{-2}$. The resulting chronopotentiometry curves are shown in Fig. 5(a) and Fig. 5(b). The overpotentials observed during the cathodic evaluation (HER) showed an initial tendency to increase and fluctuated by 115 mV, especially within the first 3 h of assessment. However, this was followed by a more stable phase in the remaining 21 h of assessment, with an overpotential around 295 mV, which is considered a low value for the applied current density. In the case of OER evaluation, overpotentials varied by less than 10 mV throughout the assessment. A gradual and continuous increase in overpotential was observed, stabilizing at approximately 298 mV, after around 13 h of polarization. This slow rise in overpotential was attributed to the accumulation and subsequent release of gas bubbles on the electrode surface, which intermittently blocked active sites and reduced the effective reaction area, thereby impacting the electrochemical performance. Once the gas bubble dynamics reached equilibrium, the system exhibited a stable overpotential.

3.2.2. Elevated temperature and pressure (ETP) assessment

The results of the NiFeP/Zn electrodes at varying temperatures (up to 80 °C) and pressures (1 and 8 bar), using the autoclave setup described in Section 2.4, are shown in Fig. 6. The catalytic response of the material was notably influenced by the increase in pressure and temperature.

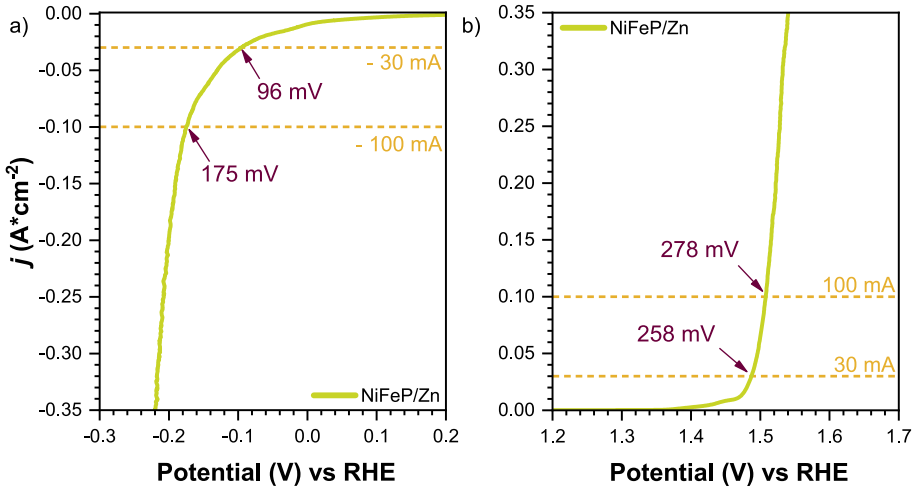

Fig. 4. Linear sweep voltammograms for NiFeP/Zn coating in 1.0 M NaOH at room laboratory conditions. a) Cathodic LSV evaluation (HER) and b) Anodic LSV evaluation (OER).

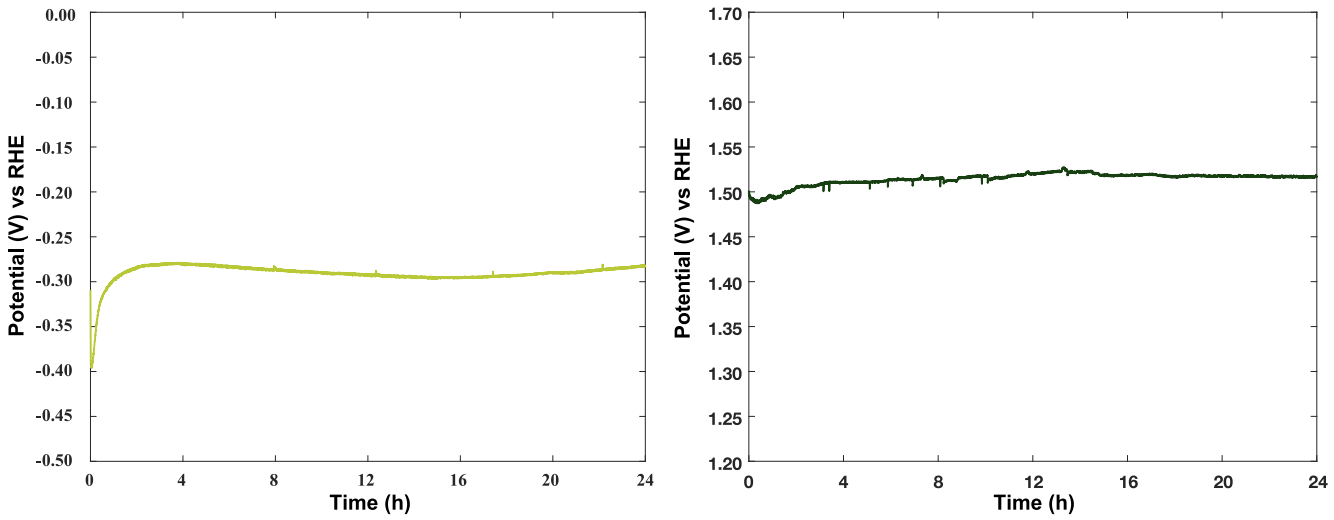

Fig. 5. NiFeP/Zn electrodes using 1.0 M NaOH and |400| $mAcm^{-2}$ a) Cathodic chronopotentiometry curve (HER) and b) Anodic chronopotentiometry curve (OER).

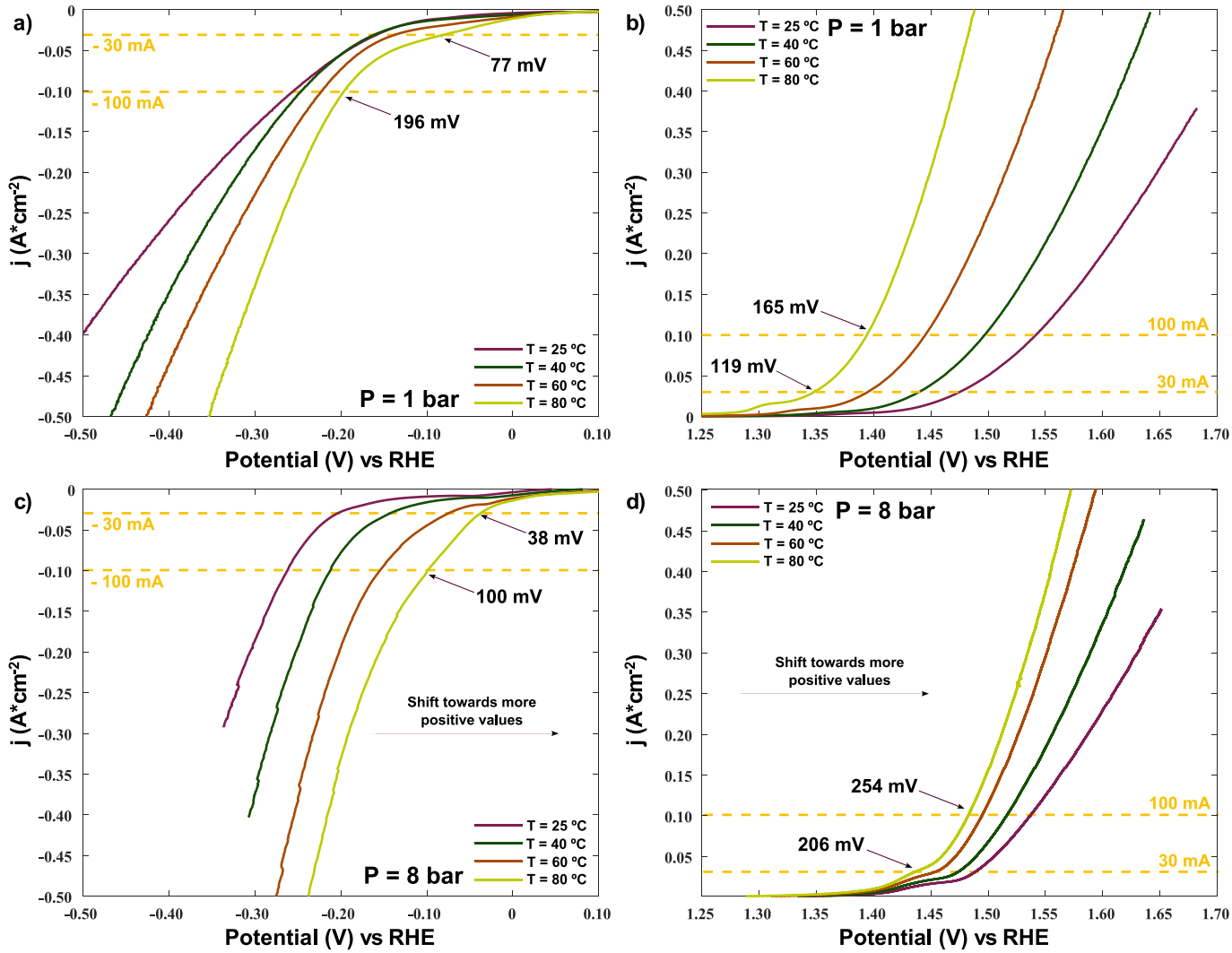

Fig. 6. Linear sweep voltammograms for NiFeP/Zn coating at different pressures and temperatures a) Cathodic LSV evaluation (HER) at 1 bar, b) Anodic LSV evaluation (OER) at 1 bar, c) Cathodic LSV evaluation (HER) at 8 bars and d) Anodic LSV evaluation (OER) at 8 bars.

This resulted in a shift towards more positive values in both cathodic and anodic water splitting reactions, showing a reduction of overpotential values for the hydrogen evolution reaction and an increase in the required overpotential in the case of the oxygen evolution reaction. A summary of the overpotentials obtained at the different conditions is presented in Fig. 7 and Table S1, in the supporting information.

The most reduced overpotential for HER was observed at the highest temperature and pressure combination (80 °C and 8 bar), with a value of 38 mV at |30| mAcm^{-2}. On the other hand, the lowest overpotential for OER was presented at the combination of highest temperature and lowest pressure (80 °C and 1 bar), with a value of 119 mV. The overall results showed a reduction in the required overpotential in both reactions compared to the results obtained at room laboratory conditions.

The effects of changes in temperature and pressure on the reversible potential have been taken into account as described in the methodology section. Pressure variations in the cell can influence gas evolution behavior in two main ways: by reducing the buoyant force due to increase in gases density, and by decreasing bubble size (according to Boyle's Law). In the latter case, this may reduce the electrode area blocked by gas bubbles, which leads to a reduce electrolyte resistance [63]. However, the second effect seems to be strongly conditioned by the nature of the evolved gas. Kitajima et al. [64] reported that, in alkaline media, oxygen evolution leads to larger bubble coverage (bigger bubbles) and greater interfacial resistance compared to hydrogen. This behavior could be attributed to the surface energy and the gas-electrode interactions specific to each gas. In the case of hydrogen, the reduction in bubble size and low gas-electrode interaction may diminish the effect of decrease buoyancy. However, in the case of oxygen, stronger interactions with the electrode may lead to increased bubble coverage at high pressures. This is supported by the LSV voltammetry results obtained at 1 bar and 8 bar, without temperature variation, where a clear increase in η is observed. Factors such as electrode morphology, surface area and wettability play a critical role in mitigating bubble-induced effects by promoting bubble detachment and increasing catalytic active sites, thereby increasing the number of nucleation points for water splitting, as other studies have mentioned [65].

Finally, the effect of increased temperature was noted through the reduction of the required overpotential for both reactions. This is possibly associated with the increase in the catalytic activity of the electrodes. As mentioned elsewhere in this study, to the best of the author's knowledge, few systems have been assessed under ETP or HTP conditions, especially under the conditions used in this study. However, a CoO_X/NF system was assessed by Leuaa et al. [25] at 150 °C and 45 bar in 45 % wt KOH for OER. The finding shows a good stabilities along prolonged assessments with overpotentials of 185 mV at 500 mA cm^{-2}.

The stability of the coating at ETP was evaluated for 24 h at an applied current density of |400| mAcm^{-2}. The evaluation was conducted under the most demanding conditions, combining a temperature of 80 °C and a pressure of 8 bar. The chronopotentiometry curves obtained under these conditions are shown in Fig. 8(a) and Fig. 8(b). For the cathodic evaluation (HER), the observed overpotential varied by 65 mV (between the lowest and highest values) and at the end of the testing time was stable at around 120 mV, which is considered a low overpotential value for the applied current density. Although small overpotential oscillations were observed throughout the test, a tendency to increase was noted during different periods. Initially, during the first 6.5 h, the potential reached 100 mV and stabilized for 1.5 h. This was followed by another increasing tendency which lasted until 16 h into the test, reaching 132 mV, after which a reduction and stabilization occurred, with the coating showing stable behavior around 115 mV until the end of the assessment. In the case of the OER evaluation, the overpotentials varied by 110 mV between the upper and lower values. The chronopotentiometry exhibited a notable increase in overpotential during the first 4 h of the test, reaching an overpotential value of 350 mV. This was followed by a decrease and a stability plateau until 20 h into the test, with a value around 334 mV. In the final stage of the assessment, an increase of 30 mV was observed in the last 4 h. The differences in stability observed under ETP compared to room conditions are attributed, particularly in the case of oxygen evolution, to a major blockage of the active sites given the interaction of oxygen with the electrode. The pronounced oscillations in both reactions were associated with the continuous accumulation and release of gas bubbles on the electrode surface, intermittently blocking active sites and thereby altering the electrochemical behavior.

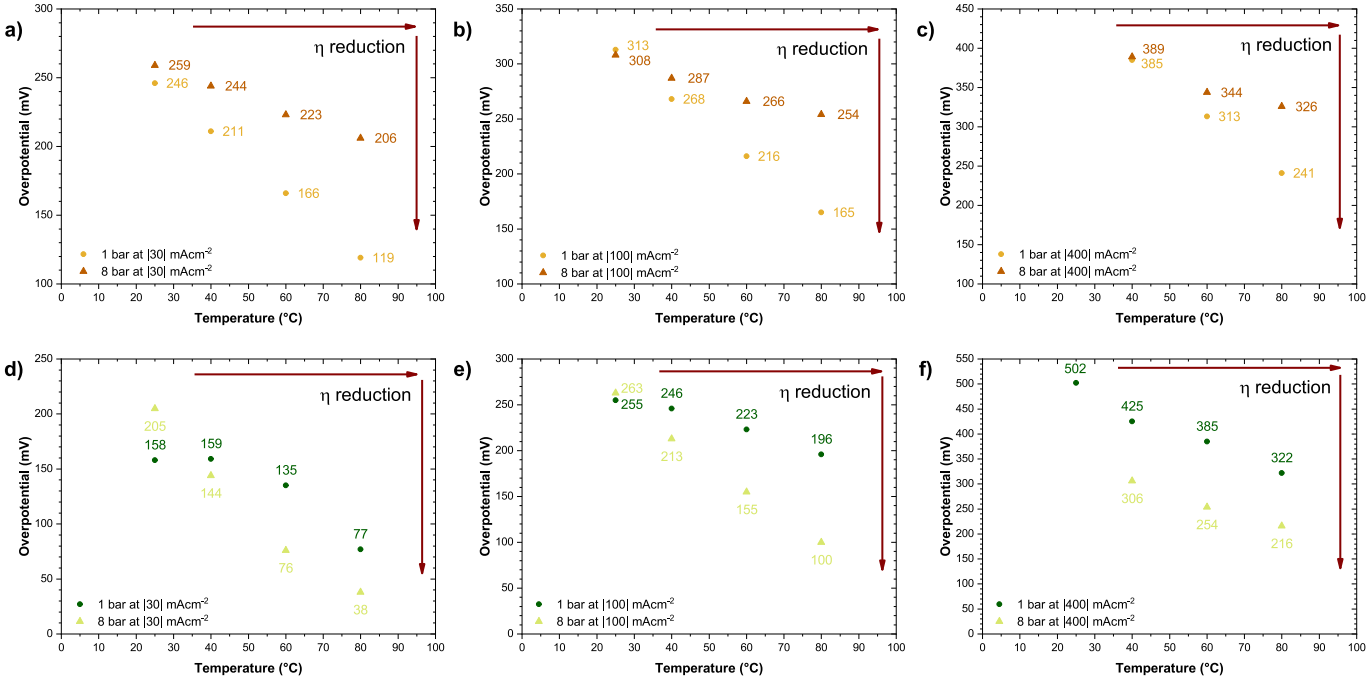

Fig. 7. Overpotential tendency associated with temperature and pressure obtained for NiFeP/Zn catalytic coatings at a) Anodic 30 mAcm^{-2}, b) Anodic 100 mAcm^{-2}, c) Anodic 400 mAcm^{-2}, d) Cathodic 30 mAcm^{-2}, e) Cathodic 100 mAcm^{-2}, f) Cathodic 400 mAcm^{-2}.

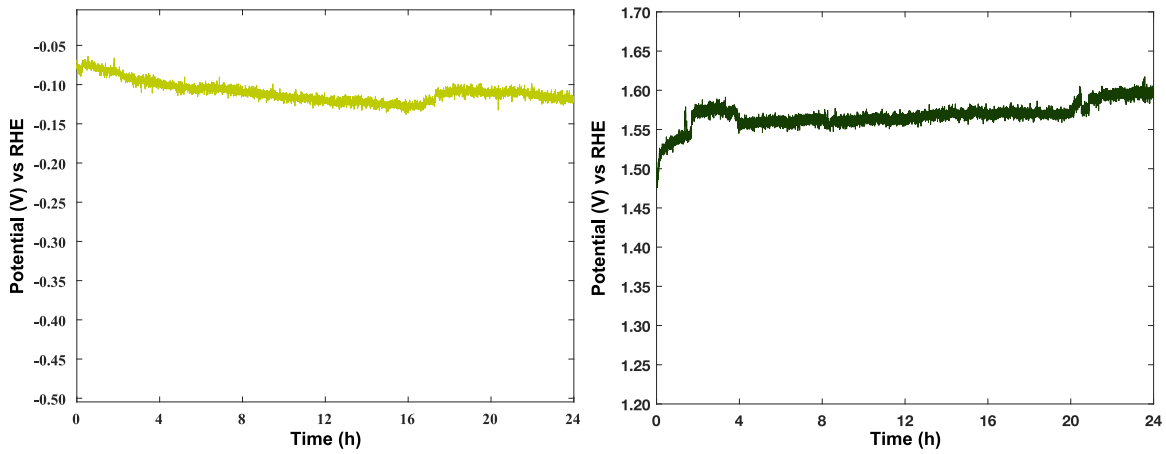

Fig. 8. NiFeP/Zn electrodes under ETP conditions using 1.0 M NaOH and |400| mAcm^{-2} a) Cathodic chronopotentiometry curve (HER) and b) Anodic chronopotentiometry curve (OER).

For better understanding of the bifunctional behavior of the NiFeP/Zn-coated Ni foams under ETP conditions, a complete cell was evaluated, using the electrodes as cathode and anode. Based on the results of the individual reactions, a full cell acting as electrolyzer and using the catalytic NiFeP/Zn coating would require a potential difference of 1.47 V to initiate water splitting at a current density of 30 mAcm^{-2} under conditions of 80 °C and 8 bar. To validate this value, additional linear sweep voltammetries were performed as full cell ETP conditions; the results are shown in Fig. 9(a) and Fig. 9(b) and the obtained potentials are also summarized in Table S2. Full cell potential values obtained at current densities of 30 mAcm^{-2} and 100 mAcm^{-2} at 80 °C and 8 bar (1.43 V and 1.64 V, respectively) were lower than those obtained at 80 °C and 1 bar (1.56 V and 1.71 V, respectively) indicating improved overall performance at elevated pressure. This behavior suggests that the previously discussed pressure-induced limitations observed for OER are mitigated by the behavior of HER kinetics under the same conditions. Consequently, the combined effect of elevated temperature and pressure in the full cell tends to reduce the overall potential. This trend was consistent across various operating conditions and aligns well with the calculated overpotentials, showing good competitiveness of the bifunctional NiFeP/Zn catalyst when compared to other works [66,67]. The obtained overpotentials are within the range of other previously reported values for advanced NiFe-based catalytic systems. Although no previous studies have reported full-cells assessments under similar ETP conditions, comparison with available literature at standard conditions can still offer insights. In a recent review [58], overall water-splitting overpotentials at |10| mAcm^{-2} in 1 M KOH were highlighted. The values ranged from 1.48 V (FM-NS NSAs) to 1.70 V (NiFe@OCC). Despite the NiFeP/Zn system being assessed at significantly higher current densities, the resulting overpotentials at ETP conditions remain competitive. This suggests that the system maintains comparable electrochemical behavior, even under more demanding operating conditions. Nevertheless, there is still room for improvement.

Full cell stability was also evaluated using chronopotentiometry over 24 h at ETP conditions, with the highest temperature and pressure combination of 80 °C and 8 bar, using a current density of 400 mAcm^{-2}. The resulting chronopotentiometry curve is shown in Fig. 10. Compared to the individual HER and OER stability curves, the full cell curve shows a significantly noisier signal with frequent potential spikes. These fluctuations are mostly associated with the constant production of bubbles on the surface of the electrodes, which accumulate and are subsequently released. This phenomenon is perceived differently in the individual chronopotentiometry curves, where the increase of overpotential due to bubble accumulation is notably slower. However, when both reactions are combined, as in this case of full cell conditions, the accumulation-release processes occur over shorter periods of time. Despite the potential jumps, a certain stability of the operational potential is observed around 1.72 V in the system, indicating general stability under the

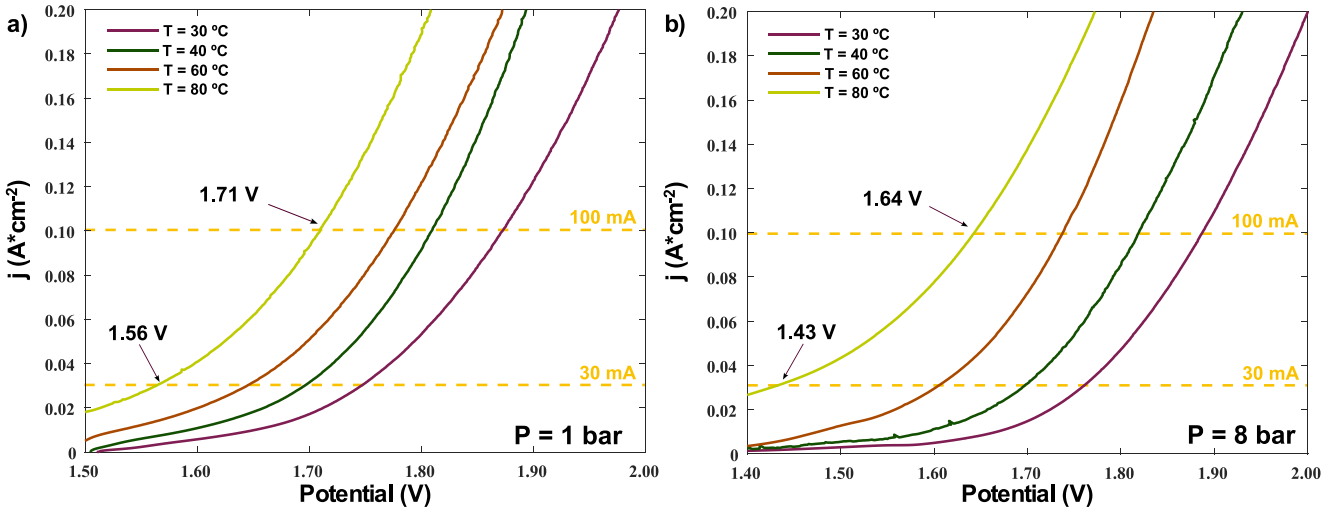

Fig. 9. Linear sweep voltammograms of Full-Cell, evaluating the NiFeP/Zn coating as bifunctional electrode at different pressures and temperatures in 1.0 M NaOH a) Evaluation at 1 bar, b) Evaluation at 8 bars.

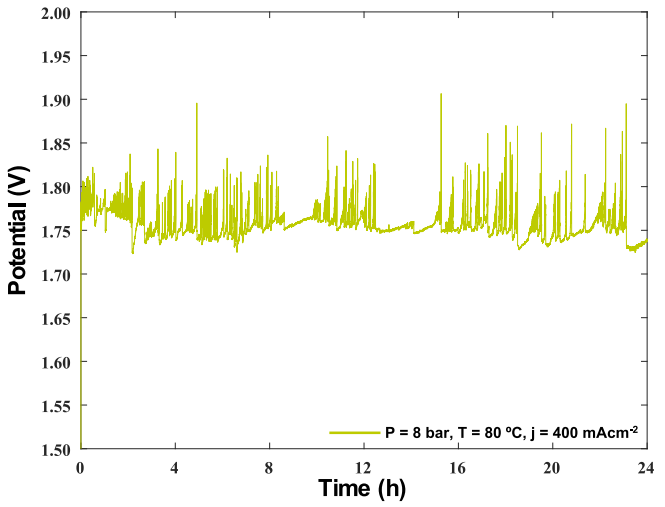

Fig. 10. Chronopotentiometry of Full-Cell, evaluating the NiFeP/Zn coating as bifunctional electrode at 80 °C, 8 bar and 400 mAcm^{-2}.

applied conditions.

3.3. Energy efficiency Determination results

An additional analysis was conducted to determine the energy efficiency of the assessed full cell and the specific energy required to produce 1 kg of H_2. This calculation was based on the electrochemical behavior observed under different ETP conditions (up to 120 °C when the pressure allowed the assessment with liquid water) using the methodology outlined in Section 2.5. The calculated efficiencies at 100 mAcm^{-2} and 200 mAcm^{-2} are shown in Fig. S3 and Table S3 in the supporting information, along with their respective specific energy consumption for hydrogen production. The resulting trend curves are shown in Fig. 11(a) and Fig. 11(b).

Fig. 11(a) shows that, regardless of the temperature or pressure, the operating efficiency of the electrolyzer is above 70 %, which confirms the outstanding catalytic activity of the NiFeP/Zn coating used. At lower temperatures, efficiency exhibits minimal variation aside from differences associated with the applied current density. Beyond the 50 °C threshold, the efficiency differences between the assessment pressures become more prominent. The efficiency at 4 bars was lower than that at 1 and 8 bar, across both assessed current densities, indicating that an initial increase in pressure reduces efficiency. However, a continuous increase in pressure leads to a more efficient system, as demonstrated by the efficiency observed at 8 bar. In the other hand, the specific energy consumption exhibits an inverse trend, with a reduction in the energy required to produce 1 kg of H2, as shown in Fig. 11(b). This tendency also indicates that the system operating at 8 bar produces H_2 with the least energy consumption.

The efficiency results for the full cell system confirm the operational reliability of the NiFeP/Zn system when it is assumed to be functioning under elevated temperature and pressure. Notably, the increase in pressure was observed to positively impact system efficiency, suggesting its relevance in practical optimization. While the behavior observed for current density and temperature corresponds with known principles of electrochemical and thermal behavior, its demonstration in practice serves to further validate the robustness of the catalytic material. Such validation is necessary in order to close the gap between laboratory-scale electrocatalyst screening and its application in real-world scenarios.

4. Conclusion

Previously developed NiFeP/Zn coatings were deposited on nickel foam electrodes, resulting in a compact morphology characterized by valleys and peaks, forming the conventional brain-like structure associated with leached Zn. Electrochemical assessment under elevated-temperature and pressure (ETP) conditions were carried out for the first time in a NiFe system to the best of the authors knowledge. This ETP assessments showed a significant reduction in the alkaline water electrolysis overpotential compared to laboratory conditions. The effects of varying temperature and pressure were studied, yielding overpotentials at $|30|$ mA cm^{-2} of 38 mV for the hydrogen evolution reaction under 8 bar and 80 °C, and 119 mV for the oxygen evolution reaction under 1 bar and 80 °C. A notable difference in the influence of the pressure on HER and OER was observed. Pressure in the cell can affect gas evolution by reducing buoyant forces and decreasing bubble size, potentially lowering the electrode area blocked by gas bubbles. However, as discussed, this second effect appears to be strongly dependent on the nature of the evolved gas, which may be attributed to differences in surface energy and gas-electrode interactions. In the case of hydrogen, the reduced bubble size may partially reduce the gas-electrode interaction, leading to less surface blockage. In contrast, oxygen bubbles may exhibit stronger interaction with the electrode, potentially resulting in increased bubble coverage at high pressures. Therefore, electrode morphology and surface wettability are considered critical factors in

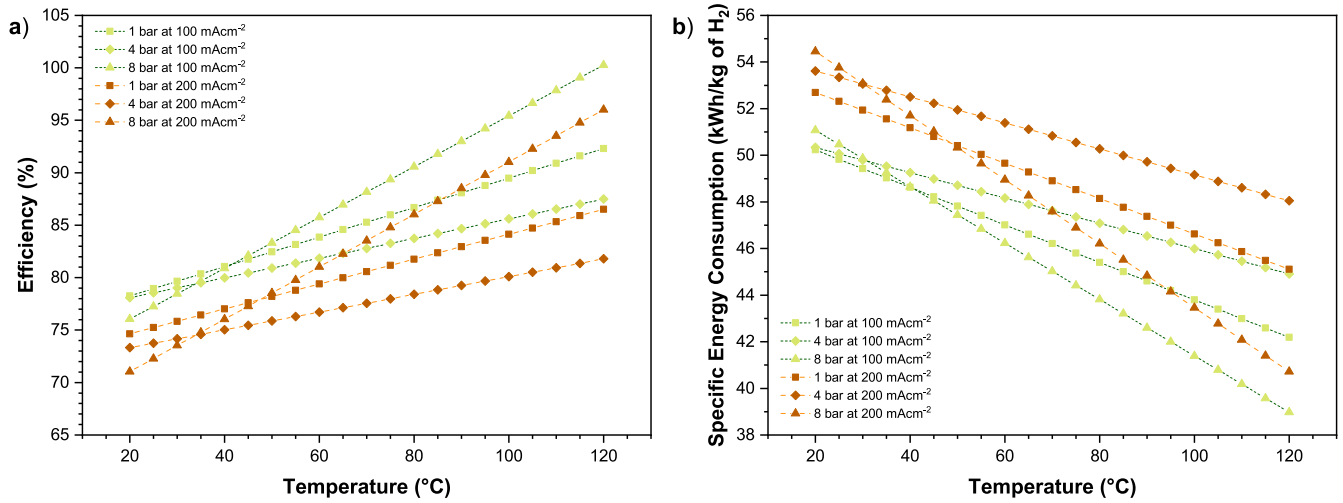

Fig. 11. Trend curves obtained for the Full-Cell system of a) Efficiency at different ETP conditions and b) Specific Energy Consumption of hydrogen production at different ETP.

enhancing the mitigation of bubble-induced effects by promoting bubble detachment, particularly for the oxygen evolution reaction. Additionally, chronopotentiometry curves demonstrated the good stability of the electrodes over 24 h at high current densities |400| mA cm^{-2}. The results were further validated by testing the electrode as a bifunctional coating in a full cell test, which showed a very low overpotential of 1.47 V at 30 mA cm^{-2} for overall water splitting. Finally, an energy efficiency analysis was performed, and the results suggested that for an electrolyzer using NiFeP/Zn coating material, pressure exhibited adverse effects at low pressures. However, increasing the pressure improved the system's energy efficiency, overcoming potential drawbacks associated with OER.

Credit Authorship Contribution Statement

Jhaniel Osorio: Investigation, Methodology and Writing. **Simón Quiroz**: Investigation. **Santiago Cartagena**: Conceptualization, Methodology, Review & Editing. **Jorge A. Calderón**: Conceptualization, Methodology, Project Administration, Funding Acquisition, Supervision, Writing-Review & Editing.

CRediT authorship contribution statement

Jhaniel Osorio: Writing – original draft, Methodology, Investigation. **Simón G. Quiroz:** Writing – original draft, Investigation. **Santiago Cartagena:** Writing – review & editing, Methodology, Conceptualization. **Jorge A. Calderón:** Writing – review & editing, Supervision, Resources, Project administration, Methodology, Conceptualization.

Declaration of competing interest

The authors declare that they have no known competing financial interests or personal relationships that could have appeared to influence the work reported in this paper.

Acknowledgments

The authors would like to thank Colombian Ministry of Science, Technology and Innovation "Minciencias" and "Sistema General de Regalías" for financial support through the scientific Program (Contract No BPIN 2022000100089).

Supplementary Materials.

Supplementary material associated with this article can be found in the online version of the paper.

Appendix A. Supplementary data

Supplementary data to this article can be found online at https://doi.org/10.1016/j.fuel.2025.136339.

Data availability

The authors declare that the data of the current manuscript are available on reasonable requests from the interest.

References

[1] Nguyen DH, Chapman A, Tsuji YT. Assessing the Optimal Contributions of Renewables and Carbon Capture and Storage toward Carbon Neutrality by 2050. Sustain 2023;15(18).
[2] Alvarez GE. Operation of pumped storage hydropower plants through optimization for power systems. Energy 2020;202:117797.
[3] Aneke M, Wang YM. Energy storage technologies and real life applications – a state of the art review. Appl Energy 2016;179:350–77.
[4] Dunn B, Kamath H, Tarascon YJM. Electrical energy storage for the grid: a battery of choices. Science (80-) 2011;334(6058):928–35.
[5] Di Sia P. Hydrogen and the State of Art of fuel Cells. J Nanosci with Adv Technol 2018;2(3):6–13.
[6] Liu W, Zuo H, Wang J, Xue Q, Ren B, Yang YF. The production and application of hydrogen in steel industry. Int J Hydrogen Energy 2021;46(17):10548–69.
[7] Griffiths S, Sovacool BK, Kim J, Bazilian M, Uratani YJM. Industrial decarbonization via hydrogen: a critical and systematic review of developments, socio-technical systems and policy options. Energy Res. Soc Sci 2021;80(August).
[8] M. Zier. Stenzel, L. Kotzur, Y D. Stolten. A review of decarbonization options for the glass industry. *Energy Convers. Manag X*. 10 May 2021 100083.
[9] Jin L, Monforti Ferrario A, Cigolotti V, Comodi YG. Evaluation of the impact of green hydrogen blending scenarios in the italian gas network: Optimal design and dynamic simulation of operation strategies. Renew Sustain Energy Transit 2022;2 (March):100022.
[10] Isaac T. HyDeploy: the UK ' s first Hydrogen Blending Deployment. Project 2019;3 (2):114–25.
[11] Yang J, et al. Electrochemistry Communications Non-precious electrocatalysts for oxygen evolution reaction in anion exchange membrane water electrolysis: a mini review. Electrochem Commun 2021;131:107118.
[12] Jang D, Choi W, Cho HS, Cho WC, Kim CH, Kang YS. Numerical modeling and analysis of the temperature effect on the performance of an alkaline water electrolysis system. J Power Sources 2021;506(May):230106.
[13] D. Jang, H. S. Cho, y S. Kang. Numerical modeling and analysis of the effect of pressure on the performance of an alkaline water electrolysis system. *Appl. Energy*. 287 (October 2020). 116554 2021.
[14] Torii K, Kodama M, Hirai YS. Three-dimensional coupling numerical simulation of two-phase flow and electrochemical phenomena in alkaline water electrolysis. Int J Hydrogen Energy 2021;46(71):35088–101.
[15] Li R, et al. Electrodeposition: Synthesis of advanced transition metal-based catalyst for hydrogen production via electrolysis of water. J Energy Chem 2021;57:547–66.
[16] Q. lv *et al.*. Controlled direct electrodeposition of crystalline NiFe/amorphous NiFe-(oxy)hydroxide on NiMo alloy as a highly efficient bifunctional electrocatalyst for overall water splitting. *Chem. Eng. J.* 446, núm. April. 137420, 2022.
[17] Zhang X-Y, Yu W-L, Zhao J, Dong B, Liu C-G, Chai YY-M. Recent development on self-supported transition metal-based catalysts for water electrolysis at large current density. Appl Mater Today 2021;22:100913.
[18] Flis-Kabulska I, Flis YJ. Electroactivity of Ni–Fe cathodes in alkaline water electrolysis and effect of corrosion. Corros Sci 2016;112:255–63.
[19] Safizadeh F, Houlachi G, Ghali YE. Electrocatalytic activity and corrosion behavior of Fe–Mo and Fe–Mo–P coatings employed as cathode material for alkaline water electrolysis. Int J Hydrogen Energy 2018;43(16):7938–45.
[20] Cartagena S, Calderón YJA. Corrosion of non-noble metal-based catalysts during oxygen evolution reaction under on/off operation. Corros Sci 2022;205:110437.
[21] Lopata JS, Kang SG, Cho HS, Kim CH, Weidner JW, Shimpalee YS. Investigating influence of geometry and operating conditions on local current, concentration, and crossover in alkaline water electrolysis using computational fluid dynamics. Electrochim Acta 2021;390:138802.
[22] Caspersen M, Kirkegaard YJB. Modelling electrolyte conductivity in a water electrolyzer cell. Int J Hydrogen Energy 2012;37(9):7436–41.
[23] Allebrod F, Chatzichristodoulou C, Mollerup L, Mogensen YM B. Electrical conductivity measurements of aqueous and immobilized potassium hydroxide. Int J Hydrogen Energy 2012;37(21):16505–14.
[24] Le Bideau D, Mandin M, Benbouzid MK, Sellier YM. Review of necessary thermophysical properties and their sensivities with temperature and electrolyte mass fractions for alkaline water electrolysis multiphysics modelling. Int J Hydrogen Energy 2019;44(10):4553–69.
[25] Leuaa P, Farzin YA, Iqbal S, Chatzichristodoulou YC. Cobalt oxide (CoOx) coated Ni foam anodes for high temperature (150 °C) and pressure (45 bar) alkaline electrolysis. J Power Sources October 2024, 2025.;625:núm.
[26] Abdelghafar F, Xu X, Jiang SP, Shao YZ. Perovskite for Electrocatalytic Oxygen Evolution at Elevated Temperatures. ChemSusChem 2024;17(15).
[27] Czioska S, et al. Heating up the OER: Investigation of IrO2 OER Catalysts as Function of potential and Temperature. ChemElectroChem 2022;9(19):1–9.
[28] Gilliam RJ, Graydon JW, Kirk DW, Thorpe Y SJ. A review of specific conductivities of potassium hydroxide solutions for various concentrations and temperatures. Int J Hydrogen Energy 2007;32(3):359–64.
[29] Ganley JC. High temperature and pressure alkaline electrolysis. Int J Hydrogen Energy 2009;34(9):3604–11.
[30] Brauns J, Turek YT. Alkaline water electrolysis powered by renewable energy: a review. Processes 2020;8(2).
[31] Khalighi F, Deen NG, Tang Y, Vreman YAW. Hydrogen bubble growth in alkaline water electrolysis: an immersed boundary simulation study. Chem Eng Sci 2023; 267:118280.
[32] Olivier P, Bourasseau C, B. Bouamama YP. Low-temperature electrolysis system modelling: a review. Renew Sustain Energy Rev 2017;78(January 2016):280–300.
[33] Roy A, Watson S, Infield YD. Comparison of electrical energy efficiency of atmospheric and high-pressure electrolysers. Int J Hydrogen Energy 2006;31(14): 1964–79.
[34] Silva JO, Cartagena S, Calderón YJ A. Novel electrodeposited NiFeP/Zn bifunctional catalytic coating for alkaline water splitting. Electrochim Acta 2023; 451:142299.
[35] Zheng W, Liu M, Lee YLYS. Best Practices in using Foam-Type Electrodes for Electrocatalytic Performance Benchmark. ACS Energy Lett 2020;5(10):3260–4.
[36] K. Sridharan y K. Sheppard. Electrodeposition of Amorphous Iron-Nickel-Phosphorus Alloy Coatings. *Trans. IMF*. 72(4), pp. 153–158, ene. 1994.
[37] AGFA. Technical Data Sheet ZIRFON PERL UTP 500. pp. 3–5, 2020.
[38] Sebbahi S, et al. A comprehensive review of recent advances in alkaline water electrolysis for hydrogen production. Int J Hydrogen Energy 2024;82(August): 583–99.
[39] M. Awad *et al.*. A review of water electrolysis for green hydrogen generation considering PV/wind/hybrid/hydropower/geothermal/tidal and wave/biogas

energy systems, economic analysis, and its application. *Alexandria Eng. J.* 87 (September 2023), pp. 213–239 2024.
[40] Onda K, Kyakuno T, Hattori K, Ito YK. Prediction of production power for high-pressure hydrogen by high-pressure water electrolysis. J Power Sources 2004;132 (1):64–70.
[41] P. Millet. Fundamentals of Water Electrolysis. *Hydrogen Production*. pp. 33–62, 13-abr-2015.
[42] LeRoy RL, Bowen CT, LeRoy YDJ. The Thermodynamics of Aqueous Water Electrolysis. J Electrochem Soc 1980;127(9):1954–62.
[43] Nickell RA, Zhu WH, Payne RU, Cahela DR, Tatarchuk YBJ. Hg/HgO electrode and hydrogen evolution potentials in aqueous sodium hydroxide. J Power Sources 2006;161(2):1217–24.
[44] Kawashima K, et al. Accurate Potentials of Hg/HgO Electrodes: Practical Parameters for Reporting Alkaline Water Electrolysis Overpotentials. ACS Catal 2023;13(3):1893–8.
[45] Balej J. Water vapour partial pressures and water activities in potassium and sodium hydroxide solutions over wide concentration and temperature ranges. Int J Hydrogen Energy 1985;10(4):233–43.
[46] Lamy C, Millet YP. A critical review on the definitions used to calculate the energy efficiency coefficients of water electrolysis cells working under near ambient temperature conditions. J Power Sources October 2019, 2020.;447:núm.
[47] Ursúa A, Marroyo L, Gubía E, Gandía LM, Diéguez M, Sanchis YP. Influence of the power supply on the energy efficiency of an alkaline water electrolyser. Int J Hydrogen Energy 2009;34(8):3221–33.
[48] Ursúa A, Gandía LM, Sanchis YP. Hydrogen production from water electrolysis: current status and future trends. Proc IEEE 2012;100(2):410–26.
[49] Koponen J, Kosonen A, Huoman K, Ahola J, Ahonen T, Ruuskanen YV. Specific energy consumption of PEM water electrolysers in atmospheric and pressurised conditions. *2016 18th Eur. Conf. Power Electron. Appl. EPE 2016 ECCE Eur.* 2016.
[50] Hernández-Gómez Á, Ramirez V, Guilbert YD. Investigation of PEM electrolyzer modeling: electrical domain, efficiency, and specific energy consumption. Int J Hydrogen Energy 2020;45(29):14625–39.
[51] Qiu Z, Ma Y, Edvinsson YT. In operando Raman investigation of Fe doping influence on catalytic NiO intermediates for enhanced overall water splitting. Nano Energy 2019;66(April):104118.
[52] Faid AY, Barnett AO, Seland F, Sunde YS. Ni/NiO nanosheets for alkaline hydrogen evolution reaction: In situ electrochemical-Raman study. Electrochim Acta 2020; 361:137040.
[53] V. I. Korepanov, S. Y. Chan, H. C. Hsu, y H. o. Hamaguchi. Phonon confinement and size effect in Raman spectra of ZnO nanoparticles. *Heliyon*. 5(2), pp. 1–14, 2019.
[54] Kong J, Fan D, Zhu. YY. Synthesis and Raman spectra of hammer-shaped ZnO nanostructures via thermal evaporation growth. Mater Sci Semicond Process 2012; 15(3):258–63.
[55] Palacio Gómez CA, Barrero Meneses CA, Jaén YJA. Raman, infrared and Mössbauer spectroscopic studies of solid-state synthesized Ni-Zn ferrites. J Magn Magn Mater 2020;505(November 2019):166710.
[56] Dzunuzovic AS, et al. Multiferroic (NiZn) Fe2O4–BaTiO3 composites prepared from nanopowders by auto-combustion method. Ceram Int 2015;41(10PartA): 13189–200.
[57] K. Shan *et al.*. Ni foam based catalysts for hydrogen evolution: from laboratory research to industrial applications. *Chem. Eng. J.* 518, núm. May, 2025.
[58] Mathew A, Rajendran S, Mathew T, Shiju NR, Rajendran S, Mathew YT. NiFe-based Electrocatalysts for Hydrogen Evolution Reaction in Alkaline Conditions: recent Trends in the Design and Structure activity Correlations. EnergyChem 2025.
[59] Chen Y, et al. Facile engineering of CoS/rGO heterostructures on carbon cloth for efficient all-pH hydrogen evolution reaction and alkaline water electrolysis. J Mater Chem A 2025;13(1):486–98.
[60] Wen J, et al. Nanostructured amorphous and nanocrystalline NiFeP composites for highly efficient oxygen evolution reaction. J Alloy Compd 2025;1025:180309.
[61] S. G. Quiroz, S. Cartagena, y J. A. Calderón. Enhancement of oxygen evolution performance of water splitting at high current density by novel electrodeposited NiFe-LDH coatings. *Electrochim. Acta*. 528(January). 2025.
[62] Xiao Z, Tang X, Gao F, Xue J, Wang YX. Exploring Ni-based alkaline OER catalysts: a comprehensive review of structures, performance, and in situ characterization methods. DeCarbon 2025;7.
[63] Sánchez M, Amores E, Rodríguez L, Clemente-Jul YC. Semi-empirical model and experimental validation for the performance evaluation of a 15 kW alkaline water electrolyzer. Int J Hydrogen Energy 2018;43(45):20332–45.
[64] Kitajima D, Misumi R, Kuroda Y, Mitsushima YS. Relationship between bubble generation behavior and hydrogen evolution reaction performance at high current densities during alkaline water electrolysis. Electrochim Acta 2024;502:144772.
[65] Fujimura T, Hikima W, Fukunaka Y, Homma YT. Analysis of the effect of surface wettability on hydrogen evolution reaction in water electrolysis using micro-patterned electrodes. Electrochem Commun 2019;101.
[66] Rahamathulla N, Murthy YAP. Advanced heterostructures as bifunctional electrocatalysts for overall water splitting - a review. J Energy Storage 2023;73 (PD):109127.
[67] Aralekallu S, Sannegowda Lokesh K, Singh YV. Advanced bifunctional catalysts for energy production by electrolysis of earth-abundant water. Fuel 2024;357(PA): 129753.